biosensors

Article

BODIPY-Based Ratiometric Fluorescent Probe for Sensing Peroxynitrite in Inflammatory Cells and Tissues

Qian Wu, Ziwei Hu, Guoyang Zhang, Yulong Jin * and Zhuo Wang *

State Key Laboratory of Chemical Resource Engineering, College of Chemistry, Beijing University of Chemical Technology, Beijing 100029, China; ac_wuqian105@163.com (Q.W.); 15608654086@163.com (Z.H.); m17863656080@163.com (G.Z.)

* Correspondence: jinyulong@buct.edu.cn (Y.J.); wangzhuo77@mail.buct.edu.cn (Z.W.)

Abstract: Peroxynitrite ($ONOO^-$) plays an important role in many physiological and pathological processes. Excessive $ONOO^-$ in cells leads to oxidative stress and inflammation. However, precise monitoring of $ONOO^-$ levels in specific organelles (e.g., mitochondria) is still lacking and urgently needed. Herein, we rationally designed a mitochondria-targeted ratiometric fluorescent probe, MOBDP-I, for imaging of $ONOO^-$ in the mitochondria of inflammatory cells and model mice. This probe, MOBDP-I, was synthesized by conjugating a BODIPY fluorophore to a mitochondria-targeting moiety–indole-salt group by a carbon–carbon double bond (C=C). In the presence of $ONOO^-$, the C=C bond between the BODIPY backbone and the indole-salt group was oxidized and broken, leading to an 18-fold enhancement of fluorescence at 510 nm, along with a significant fluorescence decrease at 596 nm. The ratiometric response property bestowed the probe with advantages in the precise quantification of $ONOO^-$ in cells, thus allowing estimation of the extent of inflammation in living cells and mouse models of rheumatoid arthritis, peritonitis, and brain inflammation. MOBDP-I could act as an effective molecular tool to study the relationship between $ONOO^-$ and the occurrence and development of inflammatory diseases.

Keywords: ratiometric probe; peroxynitrite; fluorescence imaging; inflammatory

Citation: Wu, Q.; Hu, Z.; Zhang, G.; Jin, Y.; Wang, Z. BODIPY-Based Ratiometric Fluorescent Probe for Sensing Peroxynitrite in Inflammatory Cells and Tissues. *Biosensors* **2024**, *14*, 638. https://doi.org/10.3390/bios14120638

Received: 31 October 2024
Revised: 19 December 2024
Accepted: 20 December 2024
Published: 22 December 2024

1. Introduction

Reactive nitrogen species (RNS) are highly reactive molecules produced as metabolic byproducts in biological systems and function as important cellular signaling molecules. $ONOO^-$, a type of RNS, is primarily produced in cells through the reaction of nitric oxide (NO) and the superoxide anion ($O_2^{\cdot -}$) [1]. $ONOO^-$ plays a critical role in regulating redox homeostasis, signal activation, transduction, and the normal immune response [2]. However, excessive $ONOO^-$ production can result in various disorders, including neurological, cardiovascular, and cerebrovascular diseases, cancer, inflammatory conditions, and autoimmune diseases [3–5]. $ONOO^-$ is mainly produced in mitochondria during drug-induced oxidative stress. Abnormal levels of $ONOO^-$ cause mitochondrial depolarization, leading to oxidative damage to biomolecules and ultimately resulting in cell necrosis and apoptosis [6,7]. Inflammation is a defense mechanism against injury or infection in organisms. Oxidative stress is a key feature of inflammation, often characterized by elevated levels of reactive species during the early stages of the inflammatory response [8]. Studies have shown that $ONOO^-$ is directly involved in tissue damage in patients with inflammation [9,10].

Given the high reactivity and short lifespan of $ONOO^-$, traditional histological and biochemical techniques are inadequate for assessing its dynamic changes in cells or in vivo in real time. Fluorescence imaging provides a powerful tool for non-invasive research of biological processes in cells and organisms due to its superior spatial and temporal resolution, sensitivity, and ability to detect targets in real time in complex biological systems [11–14]. Currently, numerous fluorescent probes have been developed for the specific

detection of $ONOO^-$. The recognition mechanisms of most of probes depend on specific interactions between $ONOO^-$ and certain substrates under biological conditions, such as oxidation-induced cleavage of ethylenic bonds [15], oxidation of benzoborate acid and its ester derivatives [16], oxidation-induced N-dearylation of N-aminophenol [17], oxidation of a-ketoamide derivatives [18], and oxidation of indoline-2,3-dione [19]. The recognition mechanisms not only dominate the specific reaction (reaction kinetics and sensitivity) of the probe toward $ONOO^-$, but also can efficiently tune the fluorescence output performances (emission wavelengths, fluorescence quantum yields, and fluorescence lifetimes) by various fluorescence regulation principles, such as intramolecular charge transfer (ICT), photo-induced electron transfer (PET), excited-state intramolecular proton transfer (ESIPT) and Förster resonance energy transfer (FRET) [20]. BODIPY dyes have great advantages in the detection of $ONOO^-$ due to their good chemical and optical stability, high quantum yield, and pH insensitivity. Zhang and colleagues developed a BODIPY-based fluorescent probe for selective detection of $ONOO^-$, using phenylboronic acid pinacol ester as the recognition group [21]. Han et al. reported a small-molecule probe for monitoring $ONOO^-$ levels during autophagy in cells and mice. The probe was constituted with a BODIPY fluorophore and a diphenylaniline as an $ONOO^-$ recognition site [22]. Currently, there are few BODIPY-based fluorescent probes for the detection of $ONOO^-$ in mitochondria, and most rely on single-signal intensity, making them susceptible to interference from measurement conditions and the cellular microenvironment. Ratiometric fluorescent probes, which provide detection results by measuring the ratio of two distinct emission intensities, have become a more reliable method for obtaining accurate qualitative and quantitative data due to their 'self-calibration' ability [23–25]. Therefore, the development of ratiometric fluorescent probes for visualizing $ONOO^-$ in vivo remains a critical need.

In this work, we designed and synthesized a mitochondria-targeted ratiometric fluorescent probe, MOBDP-I, for the detection of $ONOO^-$. As depicted in Scheme 1, the mitochondria-targeting moiety–indole-salt group was specifically incorporated into the BODIPY scaffold via a carbon–carbon double bond (C=C) to construct the fluorescent probe, MOBDP-I. Upon interaction with $ONOO^-$, the C=C bond between the BODIPY backbone and the indole-salt group was oxidized and broken, leading to an 18-fold enhancement of fluorescence at 510 nm, along with a significant fluorescence decrease at 596 nm. The ratio of I_{510}/I_{596} was enhanced by approximately 44-fold. More importantly, MOBDP-I was successfully employed to detect $ONOO^-$ in inflammatory cells and tissues.

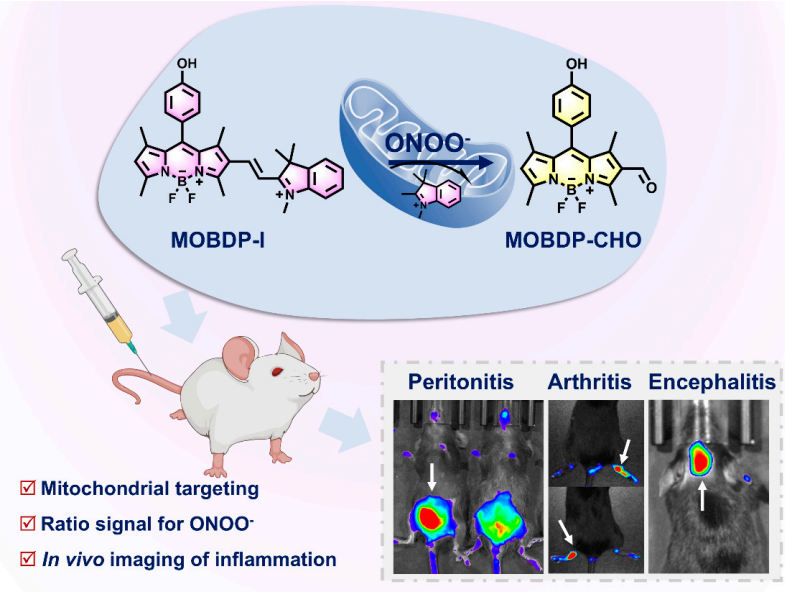

Scheme 1. The response mechanism of MOBDP-I to $ONOO^-$ and the fluorescence imaging of MOBDP-I in various inflammatory mouse models.

2. Experimental Section

2.1. Synthesis of MOBDP

4-Hydroxy benzaldehyde (0.54 g, 4.40 mmol), 2, 4-dimethylpyrrole (1.0 mL, 9.74 mmol) and a few drops of TFA were dissolved in THF (75 mL). The reaction mixture was stirred at room temperature overnight under N_2 atmosphere. DDQ (1.10 g, 4.87 mmol) was then added, and the mixture was stirred for 3 h. Afterward, Et_3N (7.5 mL) and $BF_3{\cdot}OEt_2$ (7.5 mL) were added under an ice bath, and the mixture was stirred for an additional 6 h. The solvent was then evaporated, and the residue was extracted with a saturated $NaHCO_3$ solution and DCM. The combined organic layers were evaporated under vacuum, and the crude product was purified by column chromatography (PE/EA = 20:1 to 5:1), yielding a red solid (540 mg). Yield: 38%. ^{1}H NMR (400 MHz, $CDCl_3$): δ 7.17 (d, 2H, J = 7.9 Hz), δ 6.98 (d, J = 8.1 Hz, 2H), δ 6.01 (s, 2H), δ 2.58 (s, 6H), δ 1.48 (s, 6H). MS (ESI, negative): m/z. calcd for $C_{19}H_{19}BF_2N_2O$, 340.16; found 339.2 $[M\text{-}H]^-$.

2.2. Synthesis of MOBDP-CHO

MOBDP-CHO was obtained via the Vilsmeier–Haack reaction. $POCl_3$ (3 mL) was slowly added to DMF (3 mL) and stirred at 0 °C for 5 min under N_2 atmosphere. The mixture was then stirred at room temperature for 30 min. MOBDP (85.3 mg, 0.25 mmol) was dissolved in $ClCH_2CH_2Cl$ (50 mL) and added to the mixture, which was stirred at 55 °C for 3 h. After the reaction was complete, a saturated $NaHCO_3$ solution (100 mL) was added to adjust the pH to neutral. The reaction mixture was extracted with DCM. The combined organic layers were dried over Na_2SO_4 and evaporated under vacuum. The crude product was further purified by column chromatography (DCM/EA = 25:1) to obtain MOBDP-CHO (54.1 mg). Yield: 58.6%.^{1}H NMR (400 MHz, DMSO-d_6): δ 9.96 (s, 1H), δ 7.18 (d, 2H, J = 8.5 Hz,), δ 6.96 (d, 2H, J = 8.5 Hz), δ 6.44 (s, 1H), δ 2.71 (s, 3H), δ 2.54 (s, 3H), δ 1.70 (s, 3H), δ 1.49 (s, 3H). MS (ESI, negative) m/z. calcd for $C_{20}H_{19}BF_2N_2O_2$, 368.1; found 367.1 $[M\text{-}H]^-$.

2.3. Synthesis of MOBDP-I

MOBDP-I was synthesized through a Knoevenagel condensation reaction. MOBDP-CHO (150 mg, 0.41 mmol) and 1,2,3,3-tetramethyl-3H-indole iodide (147 mg, 0.49 mmol) were dissolved in anhydrous ethanol (20 mL). The reaction mixture was refluxed at 85 °C under N_2 atmosphere for 8 h. After completion, the reaction solution was evaporated under reduced pressure. The crude product was purified by column chromatography (DCM/MeOH = 50:1 to 10:1) to obtain a violet-black solid (120 mg). Yield: 58.6%. ^{1}H NMR (400 MHz, DMSO-d_6) δ 10.02 (s, 1H), δ 8.06 (d, 1H, J = 16.3 Hz), δ 7.88–7.82 (m, 2H), δ 7.63–7.55 (m, 2H), δ 7.22 (d, J = 8.5 Hz, 2H), δ 7.00 (d, 2H, J = 8.5 Hz), δ 6.94 (d, 1H, J = 16.3 Hz), δ 6.49 (d, 1H, J = 1.2 Hz), δ 4.00 (s, 3H), δ 2.82 (s, 3H), δ 2.57 (s, 3H), δ 1.73 (s, 9H), δ 1.53 (s, 3H). ^{13}C NMR (101 MHz, DMSO) δ 182.47, 162.19, 159.18, 157.35, 155.55, 148.02, 144.87, 144.05, 143.43, 142.33, 140.52, 134.53, 134.51, 131.43, 129.75, 129.41, 129.24, 125.69, 125.62, 125.06, 123.96, 123.30, 116.77, 115.16, 111.51, 55.40, 52.89, 40.63, 40.42, 40.21, 40.01, 39.80, 39.59, 39.38, 34.45, 26.85, 15.31, 14.28, 13.62. HRMS (ESI, positive) m/z. calcd for $C_{32}H_{33}BF_2N_3O^+$ $([M]^+)$: 524.2679; found: 524.2680.

3. Result and Discussion

3.1. Design and Synthesis of Fluorescent Probe

BODIPY-based fluorescent probes have been developed for the detection of $ONOO^-$ through structural modifications of the BODIPY core [26–29]. $ONOO^-$ exhibits strong oxidizing properties, enabling the oxidation and cleavage of unsaturated bonds. This mechanism has been widely employed in the design of fluorescent probes for $ONOO^-$ sensing [30–33]. The negatively charged mitochondrial inner membrane can be targeted by the positively charged Indo group, which also exhibits strong electron-withdrawing properties. When the Indo group is conjugated to the BODIPY fluorophore via a C=C bond, the emission wavelength of the fluorescent probe is red-shifted. In this study, a BODIPY-

based, mitochondria-targeting, ratiometric fluorescent probe was synthesized according to the steps outlined in Figure S1. The detailed synthesis is described in Experimental Section. The corresponding ^{1}H NMR, ^{13}C NMR and HRMS characterizations are provided in Figures S2–S8.

3.2. Photophysical Properties and Responses to ONOO$^-$

After obtaining MOBDP-I, we began exploring its spectral properties in PBS buffer (pH 7.4, 10 mM). We first examined the absorption and fluorescence emission spectra of MOBDP-I. As shown in Figure 1a, MOBDP-I exhibited a maximum absorption peak at 550 nm and two major emission peaks at 510 nm and 596 nm. We tested the absorption spectra of MOBDP-I in various solvents at room temperature (Figure 1b). The absorption maxima of MOBDP-I in highly polar solvents such as PBS, DMSO, and methanol exhibited a red-shift relative to those in less polar solvents like DCM. MOBDP-I is a molecule with a D-π-A structure. The red-shift of MOBDP-I absorption spectra could be induced by solvent polarity, indicating that the ICT effect exists in the structure of MOBDP-I. The reaction of MOBDP-I to ONOO$^-$ was investigated at pH 7.4 in aqueous solutions. In the presence of ONOO$^-$, the absorption intensity at 550 nm decreased, and the solution color changed from purple to light pink (inset in Figure 1c), due to the oxidation of the double bond by ONOO$^-$ (Figure 1c). MOBDP-I responded to ONOO$^-$ rapidly, and the reaction completed in less than 1 s, indicating that MOBDP-I could quickly and effectively detect ONOO$^-$ (Figure 1d). As shown in Figure 2a, with increasing concentrations of ONOO$^-$, the fluorescence intensity at 596 nm decreased, while the fluorescence intensity at 510 nm gradually increased. This indicated that MOBDP-I was capable of detecting ONOO$^-$ and exhibited a ratiometric fluorescence signal. The change in ratiometric fluorescence of MOBDP-I was linearly related to the concentration of ONOO$^-$ in the range of 0 to 10 μM (Figure 2b). The correct linear equation was y = 4.564x + 0.09594, with a linear regression coefficient (R^2) of 0.9901, indicating a strong linear relationship. Based on the formula LOD = 3σ/s, the limit of detection (LOD) of MOBDP-I for ONOO$^-$ was determined to be 9.6 nM, confirming that MOBDP-I could sensitively detect ONOO$^-$.

Considering the complexity of the physiological environment and the potential impact on sensing signals, we evaluated the selectivity of MOBDP-I for various potential coexisting molecules, including reducing agents (H_2S, SO_3^{2-}, HSO_3^-, GSH, Cys), oxidants ($^1O_2$, ClO^-, H_2O_2, ROO^-, ·OH, NO_2^-, NO_3^-), and metal ions (K^+, Na^+, Ca^{2+}, Mg^{2+}, Zn^{2+}, Cu^{2+}, Ni^{2+}, Co^{2+}). As shown in Figure 2c,d, these interfering species exhibited negligible fluorescence changes compared to ONOO$^-$. Furthermore, MOBDP-I demonstrated stable ratiometric fluorescence enhancement for ONOO$^-$ even in the presence of high concentrations of interferents (Figure S9). These results confirm that MOBDP-I exhibits excellent selectivity for ONOO$^-$. In addition, the key analytical parameters of MOBDP-I (including maximum $\lambda_{ex}/\lambda_{em}$ of fluorophore, signal-to-noise ratio (SNR), detection limit, response time, and biological applications) were compared with previously reported fluorescent probes for detecting ONOO$^-$ (Table S1). The comprehensive data analysis revealed that the probe MOBDP-I exhibited superior analytical performance in terms of SNR, detection limit, response time, and biological applications. To investigate the mechanism of the reaction between MOBDP-I and ONOO$^-$, we characterized the reaction product using ESI-MS (Figure S10). The molecular weight of the product (m/z = 367.3, [M-H]$^-$) was found to be consistent with that of MOBDP-CHO. As shown in Figures S11 and S12 the emission spectrum of MOBDP-CHO matches that of the product formed in the reaction between MOBDP-I and ONOO$^-$, with the maximum emission wavelength at 510 nm. These results confirmed that ONOO$^-$ oxidatively cleaved the C=C bond of MOBDP-I, releasing the intermediate product MOBDP-CHO.

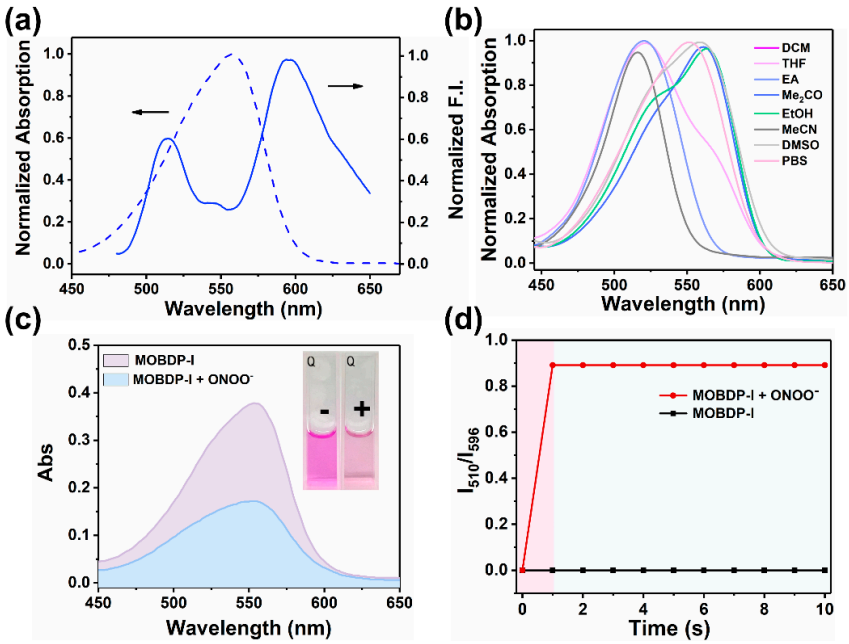

Figure 1. (**a**) UV-vis absorption and fluorescence spectra of MOBDP-I (10 μM) in PBS (10 mM, pH = 7.4, 0.1% DMSO). (**b**) Normalized absorption spectra of MOBDP-I (10 μM) in various solvents, including DCM, THF, EA, Me_2CO, EtOH, MeCN, DMSO, PBS. (**c**) Absorption spectra of MOBDP-I (10 μM) with and without $ONOO^-$ (10 μM) in PBS (pH = 7.4). Inset: − (without $ONOO^-$), + (with $ONOO^-$). (**d**) The response time of MOBDP-I (10 μM) to $ONOO^-$ (10 μM) in PBS (pH 7.4), λ_{ex} = 460 nm.

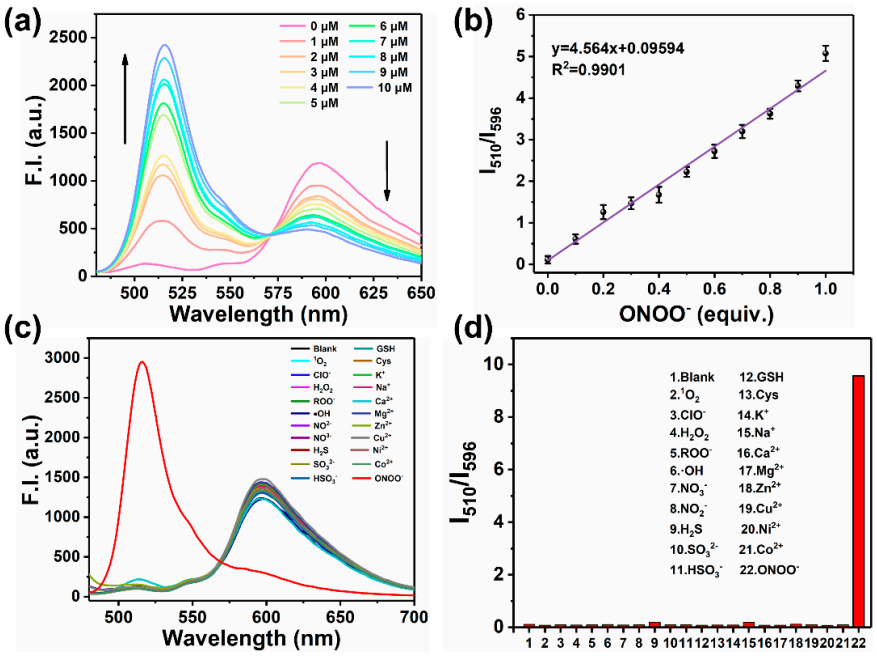

Figure 2. (**a**) Fluorescence spectra of MOBDP-I (10 μM) in response to $ONOO^-$ (0~10 μM) in PBS (pH = 7.4), λ_{ex} = 460 nm. (**b**) Linear relationship between the fluorescence intensity ratio (I_{510}/I_{596}) and $ONOO^-$ concentration from 0 to 10 μM. (**c**) Fluorescence spectra of MOBDP-I (10 μM) in the presence of 10 μM of $ONOO^-$ or 50 μM of other relevant analytes. (**d**) The fluorescence response intensity (I_{510}/I_{596}) of MOBDP-I to $ONOO^-$ (10 μM) and other relevant analytes (50 μM). Analytes: $^1O_2$, ClO^-, H_2O_2, ROO^-, ·OH, NO_3^-, NO_2^-, H_2S, SO_3^{2-}, HSO_3^-, GSH, Cys, K^+, Na^+, Ca^{2+}, Mg^{2+}, Zn^{2+}, Cu^{2+}, Ni^{2+}, Co^{2+}. Samples were measured in PBS (pH = 7.4) at room temperature with λ_{ex} = 460 nm. The error bars represent ± standard deviation (SD) (n = 3).

3.3. Mitochondrial Localization

The cytotoxicity of MOBDP-I on HeLa, RAW264.7, and PC12 cells was assessed using methyl thiazolyl tetrazolium (MTT) assay prior to cell imaging [34]. The cells survival rates remained above 80% even at a MOBDP-I concentration of 40 μM, indicating that MOBDP-I presented low cytotoxicity (Figure S13). The photostability of MOBDP-I is shown in Figure S14. After 300 s of continuous laser irradiation, the average fluorescence intensity of MOBDP-I decreased by only 24%, demonstrating good photostability and suitability for both cellular and in vivo imaging. Given that the structure of MOBDP-I contains positively charged indole-salt moieties, MOBDP-I possessed mitochondrial localization capability. Co-localization experiments were performed with the commercial mitochondrial dye Rhodamine 123 (Rh123) as a mitochondrial tracker. The mitochondrial tracker has an excitation wavelength of 488 nm and a fluorescence collection range of 510 to 540 nm. Fluorescence confocal imaging revealed a high Pearson correlation coefficient (R = 0.96, calculated by ImageJ (Version: Fiji) software) between MOBDP-I and the mitochondrial tracker (Figure 3), indicating that MOBDP-I could effectively target mitochondria.

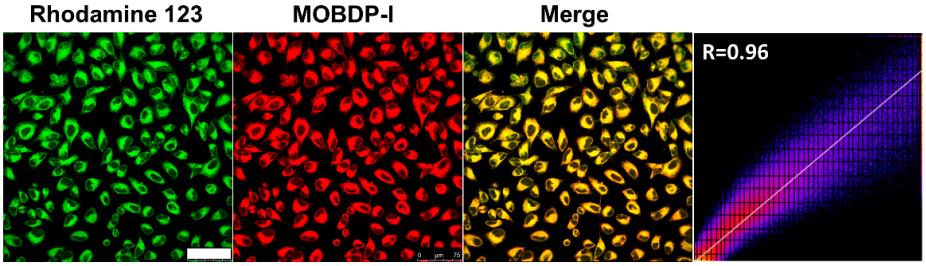

Figure 3. Co-localization imaging in HeLa cells with probe MOBDP-I (10 μM) and Rhodamine 123 (5 μM). Green channel: λ_{ex} = 488, λ_{em} = 510–540 nm. Red channel: λ_{ex} = 543, λ_{em} = 580–650 nm, scale bar: 75 μm.

3.4. Cell Imaging of Exogenous and Endogenous $ONOO^-$

Encouraged by the excellent properties of MOBDP-I for detecting $ONOO^-$ in solutions, we first investigated its ability to detect exogenous $ONOO^-$ in living cells. As shown in Figure 4a,b, when HeLa cells were incubated with only the probe MOBDP-I, the red channel exhibited obvious fluorescence, while the green channel displayed almost no fluorescence. As the concentration of $ONOO^-$ increased, the fluorescence intensity of the green channel progressively increased, while that of the red channel gradually decreased. At a concentration of 10 μM $ONOO^-$, the fluorescence intensity of the green channel was enhanced by more than 49-fold, while the fluorescence intensity of the red channel decreased by 84%. Therefore, there was a more than 310-fold enhancement in the ratiometric fluorescence intensity (Figure 4c). MOBDP-I was effective for monitoring exogenous $ONOO^-$ levels in living cells.

We further investigated the ability of MOBDP-I to detect endogenous $ONOO^-$ in cells. HeLa cells were stimulated with lipopolysaccharide (LPS) (1 μg/mL) to induce the production of endogenous $ONOO^-$. As shown in Figure 5a, control cells exhibited weak fluorescence in the green channel and strong fluorescence in the red channel after co-incubation with MOBDP-I. As the co-incubation time with LPS increased from 6 to 12 h, the fluorescence intensity of the green channel gradually increased, while that of the red channel decreased. Compared to the control group, the ratiometric fluorescence intensity of the treatment group (LPS 12 h) increased approximately 12-fold. N-acetylcysteine (NAC) effectively removed $ONOO^-$ from the cells, resulting in fluorescence intensities similar to those of the control group (Figure 5b). Similar imaging results were observed in RAW264.7 cells (Figure S15). As shown in Figure 5c, the red channel fluorescence intensity gradually decreased, while the green channel fluorescence intensity increased with increasing LPS concentrations. Quantitative analysis clearly demonstrated significant changes in the ratiometric signal of the dual-channel fluorescence intensities (Figure 5d). These results suggested that MOBDP-I can effectively monitor the levels of both endogenous and exogenous $ONOO^-$ in living cells.

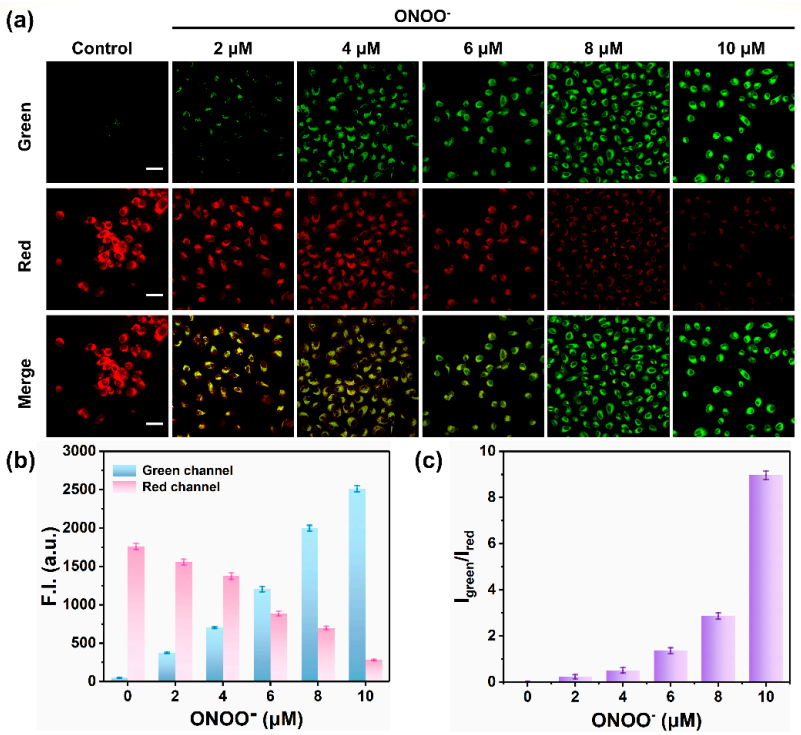

Figure 4. (**a**) Fluorescence imaging of exogenous $ONOO^-$ (0, 2, 4, 6, 8, and 10 μM) in HeLa cells stained with MOBDP-I (10 μM). scale bar: 50 μm. (**b**) Relative fluorescence intensities corresponding to panel (**a**) in both the green and red channels. (**c**) Fluorescence intensity ratio corresponding to panel (**a**). Green channel: λ_{ex} = 488 nm, λ_{em} = 510–540 nm. Red channel: λ_{ex} = 543 nm, λ_{em} = 580–650 nm. The error bars represent ± standard deviation (SD) (n = 3).

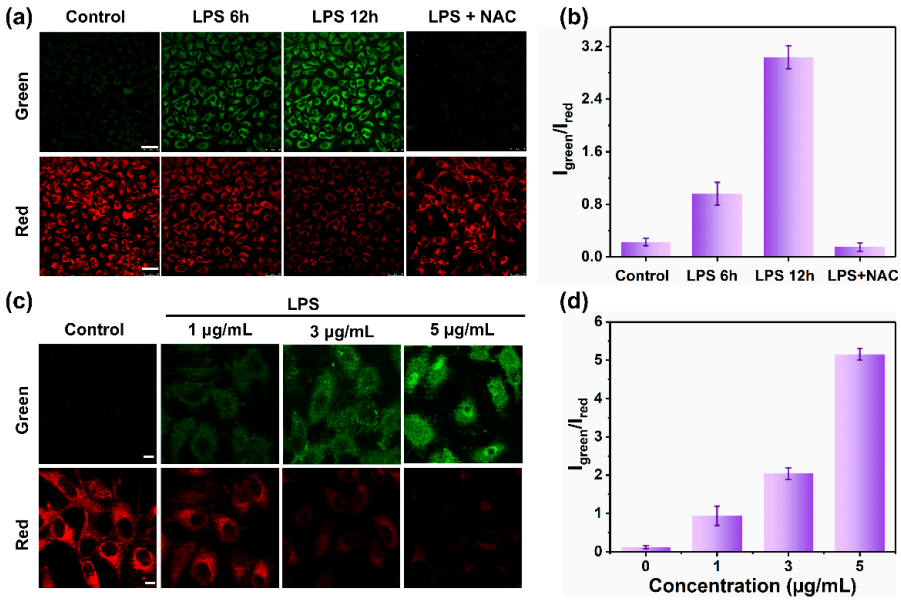

Figure 5. Fluorescence imaging of endogenous $ONOO^-$ in HeLa cells. (**a**) The cells were treated with LPS (1 μg/mL) for different times and then incubated with MOBDP-I (10 μM). Green channel: λ_{ex} = 488 nm, λ_{em} = 510–540 nm. Red channel: λ_{ex} = 543 nm, λ_{em} = 580–650 nm, scale bar: 50 μm. (**b**) Fluorescence intensity ratio corresponding to panel (**a**). (**c**) The cells were treated with different concentrations of LPS for 6 h and then incubated with MOBDP-I (10 μM). Green channel: λ_{ex} = 488 nm, λ_{em} = 510–540 nm. Red channel: λ_{ex} = 543 nm, λ_{em} = 580–650 nm, scale bar: 10 μm; (**d**) Fluorescence intensity ratio corresponding to panel (**c**). The error bars represent ± standard deviation (SD) (n = 3).

3.5. Fluorescent Imaging of $ONOO^-$ in Inflamed Mouse Model

Building on the exceptional ability of MOBDP-I to image intracellular $ONOO^-$, we further investigated its potential for in vivo imaging. Various inflammatory mouse models were applied to evaluate sensing capability. First, we assessed the imaging performance of MOBDP-I using an arthritis model. We used λ-carrageenan (λ-carr) to induce a mouse model of arthritis [35–39]. To construct the arthritis model, C57BL/6 mice were injected with λ-carr (50 μL, 5 mg/mL) in the right hindlimb joint. PBS (50 μL) was injected into the left hindlimb joint as a control group. After 8 h, the right hind limb of the mice appeared red and swollen, whereas the control group did not show this phenomenon, indicating that the arthritis model was successfully constructed. MOBDP-I (20 μM, 100 μL in 1:9 DMSO/PBS v/v) was injected and imaged with a three-dimensional optical in vivo imaging system (IVIS Spectrum). As shown in Figure 6a, in the control group, the red channel at the joint displayed clear fluorescence, while the green channel exhibited almost no signal. In contrast, the experimental group showed a reduction in the red channel fluorescence intensity, whereas the green channel intensity was significantly enhanced, resulting in a six-fold increase in the ratio of fluorescence intensities in the two channels (Figure 6b). To confirm that this phenomenon was due to $ONOO^-$ production, NAC was administered to the experimental group. The fluorescence of the red channel was restored, while the green channel fluorescence was weakened, confirming the effect of $ONOO^-$. To further investigate the broader applicability of MOBDP-I for $ONOO^-$ imaging in inflamed tissues, we established a mouse peritonitis model. As shown in Figure 6c,d, the fluorescence intensity in the green channel of LPS-injected mice was significantly higher than that of the control group, while the red channel showed a lower intensity compared to the control. This suggests that peritonitis induces an increase in $ONOO^-$. Following NAC treatment, the fluorescence intensity in the green channel markedly decreased, whereas the red channel intensity significantly increased, indicating that NAC effectively eliminated $ONOO^-$. T MOBDP-I could sense the change in $ONOO^-$ in the mouse peritonitis model.

Moreover, we were curious whether the MOBDP-I probe can be used to track the levels of $ONOO^-$ in brain inflammation. Therefore, we constructed a mouse brain inflammation model. Brain inflammation could be induced by intraperitoneal injection of LPS (2 mg/mL,100 μL) [40–43]. MOBDP-I was used to image changes in $ONOO^-$ in brain inflammation. As shown in Figure 7a,b, the fluorescence intensity in the red channel of the experimental group (right) was significantly stronger than that of the control group (left), indicating that MOBDP-I successfully crossed the blood–brain barrier and imaged $ONOO^-$ in brain-inflammation mice. During the 90 min imaging session, the fluorescence intensity initially increased and then gradually decreased. The reason for this was that the brain uptake rate of MOBDP-I exceeded its clearance rate during the first 30 min, leading to the accumulation of the probe in the brain with enhanced fluorescence. Subsequently, the fluorescence intensity gradually decreased because of brain clearance and metabolic mechanisms. However, imaging results in the green channel were not observable. The reason for this was that emission wavelength of the MOBDP-I green channel was too short to pass through the structure of the mouse skull. When mouse brains were dissected for in vitro fluorescence imaging, the signal of MOBDP-I from both green and red channels could be detected in the dissected mouse brains, with a significant increase in the fluorescence intensity of the green channel and a decrease in the red channel (Figure 7c,d). The biosafety of the probe MOBDP-I was evaluated. The hemolysis rate of MOBDP-I was relatively low (Figure S16). The metabolic distribution of MOBDP-I in various organs was examined, and histopathological analyses of the major organs were performed using H&E staining. MOBDP-I was primarily metabolized in the liver and had no significant effects on other organs (Figures S17 and S18). These results suggest that MOBDP-I possessed a favorable biosafety profile. MOBDP-I could detect $ONOO^-$ sensitively and has feasibility at the organismal level, and holds strong potential as a candidate for future clinical studies.

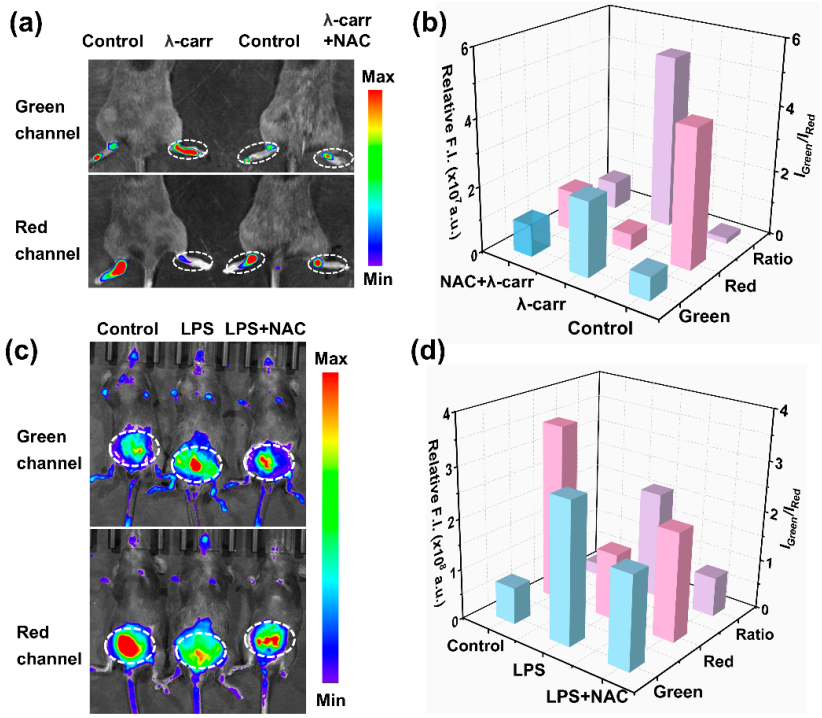

Figure 6. (**a**) Fluorescence imaging of MOBDP-I in a mouse model of rheumatoid arthritis. Control group: the left hind limb of mice, in situ injection of PBS (50 μL, 10 mM, pH = 7.0); experimental group: the right hind limb of mice, in situ injection of λ-carr (50 μL, 5 mg/mL) or λ-carr (50 μL, 5 mg/mL) + NAC (50 μL, 30 mg/kg). (**b**) Relative fluorescence intensities corresponding to panel (**a**); (**c**) Fluorescence imaging of MOBDP-I in a mouse model of peritonitis. Control group: intraperitoneal injection of PBS (50 μL, 10 mM, pH = 7.0); experimental group: intraperitoneal injection of LPS (50 μL, 2 mg/mL) or LPS (50 μL, 2 mg/mL) + NAC (50 μL, 30 mg/kg). (**d**) Relative fluorescence intensities corresponding to panel (**c**). Green channel, λ_{ex} = 460 nm, λ_{em} = 510–550 nm. Red channel, λ_{ex} = 570 nm, λ_{em} = 650–700 nm.

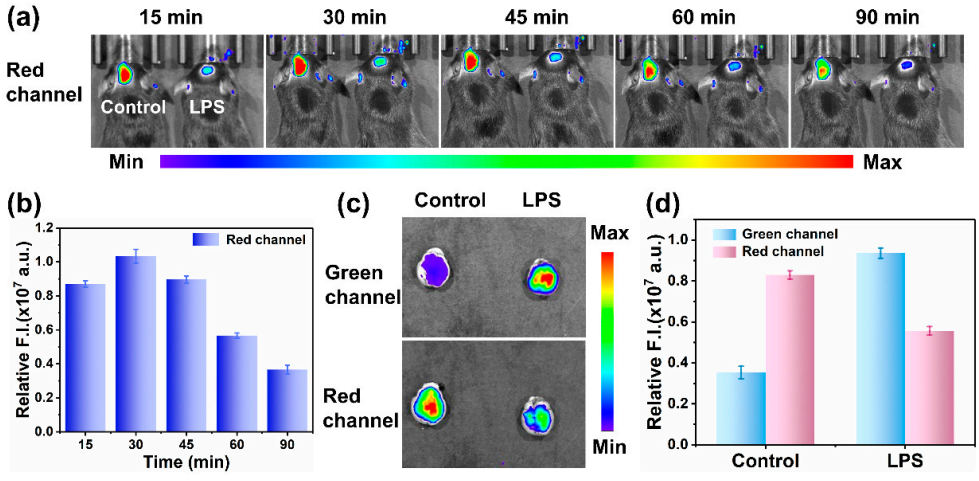

Figure 7. (**a**) Fluorescence imaging of MOBDP-I in mouse model of brain inflammation. Control group (left): tail vein injection of PBS (50 μL, 10 mM, pH = 7.0), and then MOBDP-I (20 μM, 100 μL in 1:9 DMSO/PBS v/v); experimental group (right): tail vein injection of LPS (100 μL, 2 mg/mL, 8 h), and then MOBDP-I (20 μM, 100 μL in 1:9 DMSO/PBS v/v). (**b**) Relative fluorescence intensities corresponding to the LPS-treated group in panel (**a**). Red channel, λ_{ex} = 570 nm, λ_{em} = 650–700 nm. (**c**) Fluorescence imaging of the dissected mouse brains. (**d**) Relative fluorescence intensities corresponding to panel (**c**). Green channel, λ_{ex} = 460 nm, λ_{em} =510–550 nm. Red channel, λ_{ex} = 570 nm, λ_{em} = 650–700 nm. The error bars represent ± standard deviation (SD) (n = 3).

4. Conclusions

In summary, we have developed a ratiometric sensing platform that selectively targets $ONOO^-$ in mitochondria. In vitro experiments demonstrated that MOBDP-I exhibited a significant spectral response to $ONOO^-$. In the presence of $ONOO^-$, the probe showed an enhancement of fluorescence at 510 nm, along with a fluorescence decrease at 596 nm, enabling the quantification of $ONOO^-$ levels by the ratio of fluorescence intensities from the two channels. MOBDP-I has the advantages of high anti-interference, low cytotoxicity, high sensitivity, and rapid response. Moreover, MOBDP-I can be applied for the ratiometric monitoring of mitochondrial $ONOO^-$ and assessing the mitochondrial oxidative stress status in living cells. Furthermore, in vivo experiments indicated that MOBDP-I can effectively distinguish between inflammatory and normal tissues in mouse models of rheumatoid arthritis, peritonitis, and brain inflammation. We believe MOBDP-I holds significant potential to be an effective molecular tool to study the relationship between $ONOO^-$ and the occurrence and development of inflammatory diseases.

Supplementary Materials: The following supporting information can be downloaded at: https://www.mdpi.com/article/10.3390/bios14120638/s1. Figure S1. The synthetic route of MOBDP-I. Figure S2. ^1H NMR spectrum of MOBDP in $CDCl_3$-d_4. Figure S3. ^1H NMR spectrum of MOBDP-CHO in $CDCl_3$-d_4. Figure S4. ^1H NMR spectrum of MOBDP-I in DMSO-d_6. Figure S5. ^{13}C NMR spectrum of MOBDP-I in DMSO-d_6. Figure S6. The mass spectrum (ESI) of MOBDP. Figure S7. The mass spectrum (ESI) of MOBDP-CHO. Figure S8. The mass spectrum (HRMS) of MOBDP-I. HRMS (ESI, positive) m/z. calcd for $C_{32}H_{33}BF_2N_3O^+$ ($[M]^+$): 524.2679; found: 524.2680. Figure S9. The fluorescence response intensity (I_{510}/I_{596}) of MOBDP-I to various analytes (50 μM) and $ONOO^-$ (10 μM) + analytes (50 μM). Analytes (1–20): $^1O_2$, ClO^-, H_2O_2, ROO^-, ·OH, NO_3^-, NO_2^-, H_2S, SO_3^{2-}, HSO_3^-, GSH, Cys, K^+, Na^+, Ca^{2+}, Mg^{2+}, Zn^{2+}, Cu^{2+}, Ni^{2+}, Co^{2+}. Figure S10. The reaction mechanism of MOBDP-I with $ONOO^-$ and mass spectra (ESI) of MOBDP-I and MOBDP-CHO. Note that MOBDP-I was analyzed in positive ion mode. The detected charged species was $[M]^+$, as itself is a cation. The product MOBDP-CHO was analyzed in negative ion mode. The detected charged species should be $[M\text{-}H]^-$. Figure S11. Fluorescence spectra of MOBDP-CHO (10 μM), MOBDP-I (10 μM) and MOBDP-I (10 μM) in response to $ONOO^-$ (10 μM) in PBS (pH = 7.4). Figure S12. Fluorescence spectra of MOBDP-I (10 μM), MOBDP-I (10 μM) + H_2O_2 (50 μM), MOBDP-I (10 μM) + $ONOO^-$ (10 μM) and MOBDP-I (10 μM) + H_2O_2 (50 μM) + $ONOO^-$ (10 μM). Figure S13. MTT assay of (a) HeLa cells, (b) RAW264.7 cells and (c) PC12 cells in the presence of different concentrations of MOBDP-I (0~40 μM). The error bars represent ± standard deviation (SD) (n = 3). Figure S14. (a) Photostability of MOBDP-I (10 μM) and Rhodamine 123 (5 μM) incubated with HeLa cells, the signal intensity varies with the laser bleaching time. (Red channel: λ_{ex} =543 nm, λ_{em} = 580–650 nm. Green channel: λ_{ex} = 488 nm, λ_{em} = 510–540 nm, scale bar = 50 μm). (b) Normalized intensity profiles of average intracellular signals calculated from the confocal fluorescence images in (a) by applying Image*J*. Figure S15. Confocal fluorescence imaging of $ONOO^-$ in RAW264.7 cells using the probe MOBDP-I (10 μM, 30 min). Control group: MOBDP-I only; LPS group: LPS (1 μg/mL, 6 h) then MOBDP-I; LPS + Minocycline group: LPS (1 μg/mL, 6 h), minocycline (300 μM, 2 h), then MOBDP-I; $ONOO^-$ group: exogenous $ONOO^-$ (10 μM, 30 min), then MOBDP-I. Green channel: λ_{ex} = 488 nm, λ_{em} = 510–540 nm. Red channel: λ_{ex} = 543 nm, λ_{em} = 600–650 nm, scale bar: 75 μm. Figure S16. Hemolysis rate at different concentrations of MOBDP-I (0–40 μM). Figure S17. Fluorescence imaging in the major organs (heart, liver, spleen, lung, and kidney) isolated from mice. Figure S18. Hematoxylin and eosin (H&E) staining of major organs (heart, liver, spleen, lung, and kidney) collected from mice. Table S1. Comparison of the proposed probe with other reported fluorescence probes for detecting peroxynitrite. References [15,21,43–49] are cited in Supplementary Materials.

Author Contributions: Conceptualization, Z.W. and Y.J.; methodology, Q.W. and Z.H.; software, G.Z.; validation, Q.W., Z.H. and G.Z.; formal analysis, Q.W.; investigation, Z.H.; resources, G.Z.; data curation, Q.W.; writing—original draft preparation, Q.W. and Z.H.; writing—review and editing, Z.W. and Y.J.; visualization, Y.J.; supervision, Z.W.; project administration, Z.W. and Y.J.; funding acquisition, Z.W. and Y.J. All authors have read and agreed to the published version of the manuscript.

Funding: This research was funded by Beijing Natural Science Foundation (No. 7232342, 2242027), the Natural Science Foundation of China (No. 22474007), and the Fundamental Research Funds for the Central Universities (buctrc202415).

Institutional Review Board Statement: The animal study protocol was approved by the Ethical Committee China-Japan Friendship Hospital. Protocol code: ZRDWLL230036. Approval Date: 13 July 2023.

Data Availability Statement: The data presented in this study are available on request from the corresponding author.

Conflicts of Interest: The authors declare no conflicts of interest.

References

1. Radi, R. The origins of nitric oxide and peroxynitrite research in Uruguay: 25 years of contributions to the biochemical and biomedical sciences. *Nitric Oxide* **2019**, *87*, 83–89. [CrossRef]
2. Olszewska, M.A.; Kolodziejczyk-Czepas, J.; Rutkowska, M.; Magiera, A.; Michel, P.; Rejman, M.W.; Nowak, P.; Owczarek, A. The Effect of Standardised Flower Extracts of *Sorbus aucuparia* L. on Proinflammatory Enzymes, Multiple Oxidants, and Oxidative/Nitrative Damage of Human Plasma Components In Vitro. *Oxid. Med. Cell Longev.* **2019**, *2019*, 9746358. [CrossRef]
3. De Armas, M.I.; Esteves, R.; Viera, N.; Reyes, A.M.; Mastrogiovanni, M.; Alegria, T.G.P.; Netto, L.E.S.; Tortora, V.; Radi, R.; Trujillo, M. Rapid peroxynitrite reduction by human peroxiredoxin 3: Implications for the fate of oxidants in mitochondria. *Free Radic. Biol. Med.* **2019**, *130*, 369–378. [CrossRef] [PubMed]
4. Chen, H.; Chen, X.; Luo, Y.; Shen, J. Potential molecular targets of peroxynitrite in mediating blood–brain barrier damage and haemorrhagic transformation in acute ischaemic stroke with delayed tissue plasminogen activator treatment. *Free Radic. Res.* **2018**, *52*, 1220–1239. [CrossRef] [PubMed]
5. Lei, Y.; Gao, Y.; Song, M.; Cao, W.; Sun, X. Peroxynitrite is a novel risk factor and treatment target of glaucoma. *Nitric Oxide* **2020**, *99*, 17–24. [CrossRef] [PubMed]
6. Chung, J.; Kim, H.; Li, H.; Yoon, J. Reasonably constructed NIR fluorescent probes based on dicyanoisophorone skeleton for imaging ONOO− in living cells. *Dye. Pigment.* **2021**, *195*, 109665. [CrossRef]
7. Yang, R.; He, X.; Niu, G.; Meng, F.; Lu, Q.; Liu, Z.; Yu, X. A Single Fluorescent pH Probe for Simultaneous Two-Color Visualization of Nuclei and Mitochondria and Monitoring Cell Apoptosis. *ACS Sens.* **2021**, *6*, 1552–1559. [CrossRef] [PubMed]
8. Kim, Y.E.; Kim, J. ROS-Scavenging Therapeutic Hydrogels for Modulation of the Inflammatory Response. *ACS Appl. Mater. Interfaces* **2022**, *14*, 23002–23021. [CrossRef] [PubMed]
9. Yao, Y.; Zhang, H.; Wang, Z.; Ding, J.; Wang, S.; Huang, B.; Ke, S.; Gao, C. Reactive oxygen species (ROS)-responsive biomaterials mediate tissue microenvironments and tissue regeneration. *J. Mater. Chem. B* **2019**, *7*, 5019–5037. [CrossRef]
10. Chen, X.; Jaiswal, A.; Costliow, Z.; Herbst, P.; Creasey, E.A.; Oshiro-Rapley, N.; Daly, M.J.; Carey, K.L.; Graham, D.B.; Xavier, R.J. pH sensing controls tissue inflammation by modulating cellular metabolism and endo-lysosomal function of immune cells. *Nat. Immunol.* **2022**, *23*, 1063–1075. [CrossRef]
11. Chen, B.; Li, C.; Zhang, J.; Kan, J.; Jiang, T.; Zhou, J.; Ma, H. Sensing and imaging of mitochondrial viscosity in living cells using a red fluorescent probe with a long lifetime. *Chem. Commun.* **2019**, *55*, 7410–7413. [CrossRef] [PubMed]
12. Yan, H.; Wang, Y.; Huo, F.; Yin, C. Fast-Specific Fluorescent Probes to Visualize Norepinephrine Signaling Pathways and Its Flux in the Epileptic Mice Brain. *J. Am. Chem. Soc.* **2023**, *145*, 3229–3237. [CrossRef] [PubMed]
13. Yan, L.; Gu, Q.S.; Jiang, W.L.; Tan, M.; Tan, Z.K.; Mao, G.J.; Xu, F.; Li, C.Y. Near-Infrared Fluorescent Probe with Large Stokes Shift for Imaging of Hydrogen Sulfide in Tumor-Bearing Mice. *Anal. Chem.* **2022**, *94*, 5514–5520. [CrossRef] [PubMed]
14. Fu, G.Q.; Song, Q.; Wang, Z.Q.; Chao, J.J.; Zhang, H.; Mao, G.J.; Chen, D.H.; Li, C.Y. Long-Term Imaging of Cys in Cells and Tumor Mice by a Solid-State Fluorescence Probe. *Anal. Chem.* **2023**, *95*, 17559–17567. [CrossRef] [PubMed]
15. Liu, Y.; Ma, Y.; Lin, W. Construction of a bi-functional ratiometric fluorescent probe for detection of endoplasmic reticulum viscosity and ONOO- in cells and zebrafish. *Sens. Actuators B Chem.* **2022**, *373*, 132742. [CrossRef]
16. Chen, Z.J.; Ren, W.; Wright, Q.E.; Ai, H.W. Genetically encoded fluorescent probe for the selective detection of peroxynitrite. *J. Am. Chem. Soc.* **2013**, *135*, 14940–14943. [CrossRef] [PubMed]
17. Li, J.; Lim, C.S.; Kim, G.; Kim, H.M.; Yoon, J. Highly Selective and Sensitive Two-Photon Fluorescence Probe for Endogenous Peroxynitrite Detection and Its Applications in Living Cells and Tissues. *Anal. Chem.* **2017**, *89*, 8496–8500. [CrossRef] [PubMed]
18. Yin, X.; Feng, W.; Gong, S.; Feng, G. Near-infrared fluorescent probe with rapid response and large Stokes shift for imaging peroxynitrite in living cells, zebrafish and mice. *Dye. Pigment.* **2020**, *172*, 107820. [CrossRef]
19. Cao, J.; An, W.; Reeves, A.G.; Lippert, A.R. A chemiluminescent probe for cellular peroxynitrite using a self-immolative oxidative decarbonylation reaction. *Chem. Sci.* **2018**, *9*, 2552–2558. [CrossRef]
20. Mao, Z.; Xiong, J.; Wang, P.; An, J.; Zhang, F.; Liu, Z.; Seung Kim, J. Activity-based fluorescence probes for pathophysiological peroxynitrite fluxes. *Coord. Chem. Rev.* **2022**, *454*, 214356. [CrossRef]

21. Han, R.; Ma, X.; Wang, J.; Zhang, B.; Ruan, M.; Jiao, J.; Zhao, W.; Zhang, J. Novel BODIPY-based NIR fluorescent probe with appropriate Stokes shift for diagnosis and treatment evaluation of epilepsy via imaging ONOO− fluctuation. *Sens. Actuators B Chem.* **2025**, *423*, 136766. [CrossRef]
22. Lei, Y.; Ren, W.; Wang, C.K.; Tao, R.R.; Xiang, H.J.; Feng, L.L.; Gao, Y.P.; Jiang, Q.; Li, X.; Hu, Y.; et al. Visualizing Autophagic Flux during Endothelial Injury with a Pathway-Inspired Tandem-Reaction Based Fluorogenic Probe. *Theranostics* **2019**, *9*, 5672–5680. [CrossRef] [PubMed]
23. Huang, C.; Jia, T.; Tang, M.; Yin, Q.; Zhu, W.; Zhang, C.; Yang, Y.; Jia, N.; Xu, Y.; Qian, X. Selective and ratiometric fluorescent trapping and quantification of protein vicinal dithiols and in situ dynamic tracing in living cells. *J. Am. Chem. Soc.* **2014**, *136*, 14237–14244. [CrossRef]
24. Jun, Y.W.; Wang, T.; Hwang, S.; Kim, D.; Ma, D.; Kim, K.H.; Kim, S.; Jung, J.; Ahn, K.H. A Ratiometric Two-Photon Fluorescent Probe for Tracking Lysosomal ATP: Direct In Cellulo Observation of Lysosomal Membrane Fusion Processes. *Angew. Chem. Int. Ed. Engl.* **2018**, *57*, 10142–10147. [CrossRef] [PubMed]
25. Wu, L.; Wu, I.C.; DuFort, C.C.; Carlson, M.A.; Wu, X.; Chen, L.; Kuo, C.T.; Qin, Y.; Yu, J.; Hingorani, S.R.; et al. Photostable Ratiometric Pdot Probe for in Vitro and in Vivo Imaging of Hypochlorous Acid. *J. Am. Chem. Soc.* **2017**, *139*, 6911–6918. [CrossRef]
26. Huo, Y.; Miao, J.; Fang, J.; Shi, H.; Wang, J.; Guo, W. Aromatic secondary amine-functionalized fluorescent NO probes: Improved detection sensitivity for NO and potential applications in cancer immunotherapy studies. *Chem. Sci.* **2019**, *10*, 145–152. [CrossRef]
27. Qin, S.; Lu, H.; Zhang, J.; Ji, X.; Wang, N.; Liu, J.; Zhao, W.; Wang, J. An activatable reporter for fluorescence imaging drug-induced liver injury in diverse cell lines and in vivo. *Dye. Pigment.* **2022**, *203*, 110345. [CrossRef]
28. Wang, N.; Wang, H.; Zhang, J.; Ji, X.; Su, H.; Liu, J.; Wang, J.; Zhao, W. Endogenous peroxynitrite activated fluorescent probe for revealing anti-tuberculosis drug induced hepatotoxicity. *Chin. Chem. Lett.* **2022**, *33*, 1584–1588. [CrossRef]
29. Yudhistira, T.; Mulay, S.V.; Lee, K.J.; Kim, Y.; Park, H.S.; Churchill, D.G. Thiomaleimide Functionalization for Selective Biological Fluorescence Detection of Peroxynitrite as Tested in HeLa and RAW 264.7 Cells. *Chem. Asian J.* **2017**, *12*, 1927–1934. [CrossRef] [PubMed]
30. Fu, Y.; Nie, H.; Zhang, R.; Xin, F.; Tian, Y.; Jing, J.; Zhang, X. An ESIPT based naphthalimide chemosensor for visualizing endogenous ONOO(-) in living cells. *RSC Adv.* **2018**, *8*, 1826–1832. [CrossRef]
31. Hou, T.; Zhang, K.; Kang, X.; Guo, X.; Du, L.; Chen, X.; Yu, L.; Yue, J.; Ge, H.; Liu, Y.; et al. Sensitive detection and imaging of endogenous peroxynitrite using a benzo[d]thiazole derived cyanine probe. *Talanta* **2019**, *196*, 345–351. [CrossRef]
32. Lu, J.; Li, Z.; Zheng, X.; Tan, J.; Ji, Z.; Sun, Z.; You, J. A rapid response near-infrared ratiometric fluorescent probe for the real-time tracking of peroxynitrite for pathological diagnosis and therapeutic assessment in a rheumatoid arthritis model. *J. Mater. Chem. B* **2020**, *8*, 9343–9350. [CrossRef]
33. Zhang, J.; Kan, J.; Sun, Y.; Won, M.; Kim, J.H.; Zhang, W.; Zhou, J.; Qian, Z.; Kim, J.S. Nanoliposomal Ratiometric Fluorescent Probe toward ONOO(-) Flux. *ACS Appl. Bio Mater.* **2021**, *4*, 2080–2088. [CrossRef] [PubMed]
34. Ma, L.; Yang, S.; Ma, Y.; Chen, Y.; Wang, Z.; James, T.D.; Wang, X.; Wang, Z. Benzothiazolium Derivative-Capped Silica Nanocomposites for beta-Amyloid Imaging In Vivo. *Anal. Chem.* **2021**, *93*, 12617–12627. [CrossRef] [PubMed]
35. Feng, H.; Zhang, Z.; Meng, Q.; Jia, H.; Wang, Y.; Zhang, R. Rapid Response Fluorescence Probe Enabled In Vivo Diagnosis and Assessing Treatment Response of Hypochlorous Acid-Mediated Rheumatoid Arthritis. *Adv. Sci.* **2018**, *5*, 1800397. [CrossRef] [PubMed]
36. Gao, M.; Zhang, X.; Wang, Y.; Liu, Q.; Yu, F.; Huang, Y.; Ding, C.; Chen, L. Sequential Detection of Superoxide Anion and Hydrogen Polysulfides under Hypoxic Stress via a Spectral-Response-Separated Fluorescent Probe Functioned with a Nitrobenzene Derivative. *Anal. Chem.* **2019**, *91*, 7774–7781. [CrossRef] [PubMed]
37. Li, Z.; Lu, J.; Pang, Q.; You, J. Construction of a near-infrared fluorescent probe for ratiometric imaging of peroxynitrite during tumor progression. *Analyst* **2021**, *146*, 5204–5211. [CrossRef] [PubMed]
38. Mao, G.J.; Wang, Y.Y.; Dong, W.P.; Meng, H.M.; Wang, Q.Q.; Luo, X.F.; Li, Y.; Zhang, G. A lysosome-targetable two-photon excited near-infrared fluorescent probe for visualizing hypochlorous acid-involved arthritis and its treatment. *Spectrochim. Acta A Mol. Biomol. Spectrosc.* **2021**, *249*, 119326. [CrossRef] [PubMed]
39. Wu, P.; Zhu, Y.; Chen, L.; Tian, Y.; Xiong, H. A Fast-Responsive OFF-ON Near-Infrared-II Fluorescent Probe for In Vivo Detection of Hypochlorous Acid in Rheumatoid Arthritis. *Anal. Chem.* **2021**, *93*, 13014–13021. [CrossRef]
40. Batista, C.R.A.; Gomes, G.F.; Candelario-Jalil, E.; Fiebich, B.L.; de Oliveira, A.C.P. Lipopolysaccharide-Induced Neuroinflammation as a Bridge to Understand Neurodegeneration. *Int. J. Mol. Sci.* **2019**, *20*, 2293. [CrossRef] [PubMed]
41. Kim, K.H.; Kim, S.J.; Singha, S.; Yang, Y.J.; Park, S.K.; Ahn, K.H. Ratiometric Detection of Hypochlorous Acid in Brain Tissues of Neuroinflammation and Maternal Immune Activation Models with a Deep-Red/Near-Infrared Emitting Probe. *ACS Sens.* **2021**, *6*, 3253–3261. [CrossRef] [PubMed]
42. Wang, H.S.; Zhang, X.F.; Dong, H.; Chen, Q.; Cao, X.Q.; Shen, S.L. Activatable near-infrared fluorescent probe triggered by nitroreductase for in vivo ulcerative colitis hypoxia imaging. *Anal. Chim. Acta* **2022**, *1221*, 340107. [CrossRef] [PubMed]
43. Yasukawa, K.; Hirago, A.; Yamada, K.; Tun, X.; Ohkuma, K.; Utsumi, H. In vivo redox imaging of dextran sodium sulfate-induced colitis in mice using Overhauser-enhanced magnetic resonance imaging. *Free Radic. Biol. Med.* **2019**, *136*, 1–11. [CrossRef]
44. Xu, W.; Yang, Q.; Zeng, J.; Tan, L.; Zhou, L.; Peng, L.; Zhou, Y.; Xie, C.; Luo, K.; Zhang, Z. A biomarker ($ONOO^-$)-activated multicolor fluorescent probe for early detection and assessment of arthritis. *Sens. Actuators B Chem.* **2022**, *359*, 131565. [CrossRef]

45. Wang, Z.; Wang, W.; Wang, P.; Song, X.; Mao, Z.; Liu, Z. Highly Sensitive Near-Infrared Imaging of Peroxynitrite Fluxes in Inflammation Progress. *Anal. Chem.* **2021**, *93*, 3035–3041. [CrossRef] [PubMed]
46. Sun, Y.; Tang, X.; Li, X.; Kong, X.; Tian, M.; Wang, Y.; Dong, B. PET-ESIPT-based fluorescent probes for revealing the fluctuation of peroxynitrite ($ONOO^-$) in living cells, zebrafishes and brain tissues. *Sens. Actuators B Chem.* **2022**, *353*, 131121. [CrossRef]
47. Qin, S.; Ran, Y.; He, Y.; Lu, X.; Wang, J.; Zhao, W.; Zhang, J. Near-Infrared Fluorescence Probe for Visualizing Fluctuations of Peroxynitrite in Living Cells and Inflammatory Mouse Models. *Chemosensors* **2023**, *11*, 316. [CrossRef]
48. Zhou, D.Y.; Li, Y.; Jiang, W.L.; Tian, Y.; Fei, J.; Li, C.Y. A ratiometric fluorescent probe for peroxynitrite prepared by de novo synthesis and its application in assessing the mitochondrial oxidative stress status in cells and in vivo. *Chem. Commun.* **2018**, *54*, 11590–11593. [CrossRef] [PubMed]
49. Luo, X.; Cheng, Z.; Wang, R.; Yu, F. Indication of Dynamic Peroxynitrite Fluctuations in the Rat Epilepsy Model with a Near-Infrared Two-Photon Fluorescent Probe. *Anal. Chem.* **2021**, *93*, 2490–2499. [CrossRef] [PubMed]